Terrain-Driven Uplink Localization in Mountainous Environments Based on Moving UAV Anchors

Hanni Yu†, Gengjun Huang†, Yi Zhang†‡*, Wenqian Cao†, Lintao Chen†,

†Department of Information and Communication Engineering, School of Informatics, Xiamen University, China
‡Key Laboratory of Multimedia Trusted Perception and Efficient Computing, Ministry of Education of China, Xiamen University, China
* Corresponding Author: yizhang@xmu.edu.cn

Abstract—**In complex mountainous areas, global navigation satellite system (GNSS) signals suffer severe degradation due to multipath and non-line-of-sight propagation. Although unmanned aerial vehicles, as part of Non-terrestrial Networks, can enhance Internet of Things (IoT)-enabled emergency localization through line-of-sight connectivity, current approaches often neglect the influence of terrain on signal behavior in machine-type communication scenarios. To address this, we propose a Terrain-Driven Uplink Localization (TDUL) framework that integrates a high-fidelity channel model based on digital elevation models and ray tracing. By simulating 5G New Radio uplink, TDUL extracts terrain features and multipath characteristics to train a Terrain-Driven XGBoost (TD-XGBoost) model, which guides a particle filter using a Student's t-distribution for robust outlier resistance. Simulation results show substantial performance gains over baseline methods across diverse altitudes and ranges, with cross-terrain evaluation demonstrating strong generalization.**

Index Terms—**Mountainous environments, unmanned aerial vehicle (UAV), non-terrestrial networks, localization.**

I. INTRODUCTION

In mountainous post-disaster scenarios, the critical golden-72-hour rescue window requires rapid and reliable localization—yet this is severely challenged by global navigation satellite system (GNSS)-denied conditions induced by complex terrain and dense vegetation. Unmanned aerial vehicles (UAVs) offer a promising solution for Internet of Things (IoT)-enabled emergency response, serving as highly mobile aerial platforms capable of establishing line-of-sight (LoS) links [1].

Integrated localization and communication systems enable dual-functional UAV operation by concurrently providing localization and communication services. [2], [3] established a reliability framework and anti-jamming techniques using a hybrid two-way ranging/time difference of arrival method, whereas [4], [5] enhanced deployment strategies via geometric analysis and age of information scheduling. A reconfigurable intelligent surface-UAV fusion approach jointly optimizes trajectory and phase to balance spectral efficiency with localization accuracy [6]. Although deep learning methods such as LocUNet [7] utilize radio maps for urban localization, their generalization across varied terrains remains unexamined.

Trajectory optimization methods exploit UAV mobility via intelligent path planning to improve localization accuracy in dynamic IoT environments. For example, Q-learning [8] facilitates autonomous learning of optimal received signal strength (RSS)-based trajectories. Likewise, [9] employed particle swarm optimization with map data for 3D trajectory design, leveraging the Fisher information matrix to expedite convergence. Further approaches include multi-stage trajectory design utilizing iterative algorithms such as gradient descent and convex approximation to achieve communication-localization trade-offs [10], [11]. Dynamic tracking methods, relying on radio maps and particle filtering, additionally exhibit adaptability in time-varying IoT environments [12].

UAV deployment and resource allocation strategies optimize static or dynamic UAV localization to maximize coverage and accuracy for IoT connectivity. For example, [13], [14] employed urban map data and linear-complexity algorithms for occlusion-aware 3D deployment. Similarly, [15] established mean squared error bounds and utilized genetic algorithms for joint position and power optimization. Although these methods typically integrate convex optimization or heuristic search to manage non-convex constraints, their effectiveness is often compromised by coverage blind spots and significant localization accuracy degradation, especially under severe shadowing from multipath occlusion.

However, existing methods often fail in mountainous IoT deployment environments due to complex terrain causing non-line-of-sight (NLoS) conditions, which systematically bias the signal measurements used by conventional localization techniques. To mitigate this issue, we propose a Terrain-Driven Uplink Localization (TDUL) framework:

- A high-fidelity channel-simulation pipeline is developed, integrating digital elevation model (DEM) with ray tracing (RT) to generate physically grounded multipath channel impulse responses (CIRs) within a 5G New Radio (NR) orthogonal frequency division multiplexing (OFDM) system.
- A Terrain-Driven XGBoost (TD-XGBoost) model is trained to map terrain and geometric features to multipath parameters, thereby capturing terrain–channel coupling and providing calibrated prediction uncertainty.
- The learned mapping is incorporated into a robust Bayesian localization algorithm: measurement residuals are formed by a particle filter using the TD-XGBoost outputs, and those residuals are modeled with a Student's t-

This work was supported by the National Natural Science Foundation of China under Grants 62401485 and the Fundamental Research Funds for the Central Universities of China under Grants 20720250028.

distribution to enhance robustness against outliers caused by NLoS and anomalous multipath.

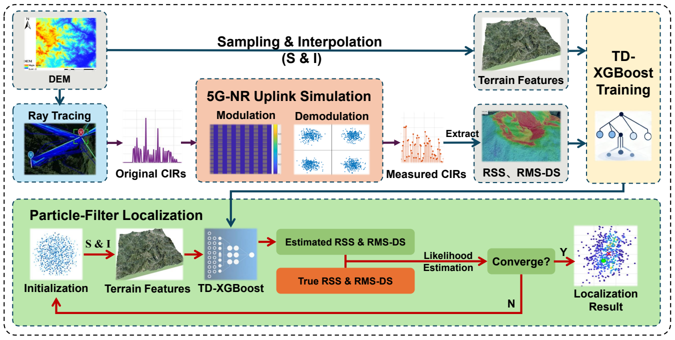

Fig. 1. Terrain-Driven Uplink Localization (TDUL) framework

II. SYSTEM MODEL

As shown in Fig. 1, the proposed TDUL framework comprises four principal modules: CIR Data Generation with RT, 5G-NR OFDM modulation/demodulation, TD-XGBoost model and particle-filter localization. The first two modules are described in this section, while the remaining two are presented in Section III.

A. System Scenario

In mountainous environments, it is assumed that both the user equipment (UE), which may be an IoT device or a mobile device, and a UAV, acting as a non-terrestrial node, are equipped with GNSS modules to acquire position data. Nevertheless, the UE's position is typically imprecise due to terrain blockage, NLoS propagation, and unfavorable satellite geometry in valleys. Accordingly, UE's actual position $\mathbf{p}_u = [x_u, y_u, z_u]$ is modeled as uniformly distributed within a sphere centered at the estimated position $\hat{\mathbf{p}}_u = [\hat{x}_u, \hat{y}_u, \hat{z}_u]$ with radius r_{err}. Thus, we define the uncertainty region Ψ_u for the UE's position as:

$$\Psi_u \triangleq \left\{ \mathbf{p}_u \in \mathbb{R}^{1\times 3} \mid (\mathbf{p}_u - \hat{\mathbf{p}}_u)(\mathbf{p}_u - \hat{\mathbf{p}}_u)^T \leq r_{\text{err}}^2 \right\} \tag{1}$$

where r_{err} depends on GNSS localization accuracy under terrain constraints. In contrast, the UAV, as part of an Non-terrestrial Network-assisted IoT infrastructure, optimizes its trajectory to maintain reliable GNSS reception, enabling it to accurately determine its own position $\mathbf{p}_a = [x_a, y_a, z_a]$ and acquire 5G-NR uplink signals from the UE for subsequent Machine-to-Machine (M2M) localization.

B. Wireless Multipath Channel Model

Electromagnetic wave propagation is jointly determined by the Earth's geometry, the propagation medium, and terrain. For example, the Earth's curvature and topography give rise to phenomena such as spherical-Earth diffraction, multipath interference, and obstacle diffraction. Because atmospheric gases and water vapor add negligible attenuation at low frequencies, this paper focuses primarily on the effects of terrain variations.

The signal path loss approaches free-space values only when the first Fresnel zone between transmitter and receiver is unobstructed by terrain obstacles. In this paper, we model the mountainous channel $h(t)$ as a composite channel comprising both large-scale and small-scale fading:

$$h(t) = \underbrace{\beta \cdot d^{-\alpha}}_{\text{Path Loss}} \cdot \underbrace{\xi_{\text{sh}}}_{\text{Shadow Fading}} \cdot \underbrace{\sum_{k=0}^{K-1} \gamma_k e^{j\phi_k} \delta(t - \tau_k)}_{\text{Multipath Components}} \tag{2}$$

where β is a frequency-dependent constant representing path loss at the reference distance (typically 1m), d is the propagation distance, α is the path loss exponent, $\xi_{\text{sh}} \sim \mathcal{LN}(0, \sigma_{\text{sh}}^2)$ denotes lognormal shadow fading. K is the number of multipaths, and γ_k, ϕ_k, and τ_k are the gain, phase, and delay of the k-th path, respectively. The model is generated by RT, which explicitly accounts for terrain undulations, vegetation blockage, and surface features.

C. CIR Data Generation with RT

DEM represents terrain topography by a discrete set of 3D vectors $\{X, Y, Z\}$, where (X, Y) are geodetic coordinates and Z denotes elevation. We employ Shuttle Radar Topography Mission data at a spatial resolution of 1 arc-second. RT computes propagation loss, delay, and phase by simulating radio-wave reflection, refraction, and diffraction phenomena. The electric field at the receiver UAV position $\mathbf{P}_a$ is

$$\mathbf{E}(\mathbf{P}_a) = \sum_{i=1}^{I} \mathbf{E}_i^{\text{dir}} + \sum_{r=1}^{R} \mathbf{E}_r^{\text{ref}} + \sum_{d=1}^{D} \mathbf{E}_d^{\text{diff}} \tag{3}$$

where $\mathbf{E}_i^{\text{dir}}$, $\mathbf{E}_r^{\text{ref}}$, and $\mathbf{E}_d^{\text{diff}}$ denote the electric field components for the direct, reflected, and diffracted paths, respectively. I, R, and D denote the numbers of direct, reflected, and diffracted rays, respectively.

The CIR represents the spatio-temporal channel response to a Dirac delta excitation $\delta(t)$. The RT computes the discrete multipath CIR for the target user and UAV as follows:

$$h(n) = \sum_{k=1}^{K} \alpha_k e^{j\phi_k} \delta(n - \tau_k) \tag{4}$$

where, for each path k, α_k is the complex attenuation factor, ϕ_k is the phase shift, and τ_k is the propagation delay. The path gain is derived from the RT path loss L_k via

$$\alpha_k = 10^{-L_k/20} \tag{5}$$

Unlike stochastic phase-modeling approaches, our implementation uses physically computed phase shifts ϕ_k from the Ray Tracer toolbox. The phase term comprises contributions from propagation delay and interaction-induced phase shifts:

$$\phi_k = \underbrace{2\pi f_c \tau_k}_{\text{propagation}} + \underbrace{\sum_{r=1}^{R} \phi_r^{\text{ref}} + \sum_{d=1}^{D} \phi_d^{\text{diff}}}_{\text{interactions}} \tag{6}$$

where f_c denotes the carrier frequency, ϕ_r^{ref} and ϕ_d^{diff} denote the phase shifts caused by the r-th reflection and the d-th diffraction, respectively, expressed in radians. These shifts depend on the material properties of the reflecting surface and the geometric characteristics of the diffraction edge.

D. 5G-NR Uplink Simulation

In practical mountainous localization systems, multipath parameter estimation is sensitive to measurement noise and sampling rate. To increase experimental realism, we generate the multipath CIR and implement an OFDM-based channel detector to acquire CIR measurements. An OFDM system with N subcarriers and an inter-subcarrier spacing of Δf has a continuous-time OFDM signal that can be expressed as:

$$s(t) = \frac{1}{\sqrt{N}} \sum_{k=0}^{N-1} S(k) \cdot \mathrm{rect}\left(t - \frac{NT}{2}\right) \cdot e^{j2\pi f_k t} \tag{7}$$

where $S(k)$ denotes the quadrature phase shift keying (QPSK) modulated symbol transmitted on the k-th subcarrier, $f_k = k \cdot \Delta f$ is the kth subcarrier frequency, T is the symbol period, and $\mathrm{rect}(t)$ is the rectangular window function defined as 1 on $[0, T]$ and 0 elsewhere.

$$x[n] = \frac{1}{\sqrt{N}} \sum_{k=0}^{N-1} S[k] e^{j2\pi kn/N}, \quad 0 \le n \le N-1 \tag{8}$$

Signals propagate through multipath channels, and the received signal can be expressed as:

$$y(t) = \sum_{k=0}^{K-1} \alpha_k s(t - \tau_k) + n(t) \tag{9}$$

where α_k and τ_k denote the complex gain and delay of the kth path, respectively, K is the total number of paths, and $n(t)$ is additive white Gaussian noise satisfying $n(t) \sim \mathcal{CN}(0, \sigma_n^2)$. We employ a comb-shaped pilot structure for channel estimation. Pilot symbols are inserted in frequency every Δk subcarriers and in time every Δl symbols. Denote the pilot-position set by $\mathcal{P}$. At the receiver, least squares channel estimation is performed at pilot positions:

$$\hat{H}[k, l] = \frac{Y_k[k, l]}{X_k[k, l]}, \quad (k, l) \in \mathcal{P} \tag{10}$$

where $Y_p[k, l]$ and $X_p[k, l]$ are the received and transmitted pilot symbols, respectively.

To obtain the channel frequency response (CFR) across all subcarriers, we apply bilinear interpolation. For non-pilot positions (k, l), identify the four nearest pilots: (k_1, l_1), (k_2, l_1), (k_1, l_2), and (k_2, l_2). The interpolated CFR is:

$$\begin{aligned} \hat{H}[k, l] = {} & (1 - \alpha)(1 - \beta)\hat{H}[k_1, l_1] + \alpha(1 - \beta)\hat{H}[k_2, l_1] \\ & + (1 - \alpha)\beta\hat{H}[k_1, l_2] + \alpha\beta\hat{H}[k_2, l_2] \end{aligned} \tag{11}$$

where $\alpha = \frac{k - k_1}{k_2 - k_1}$ and $\beta = \frac{l - l_1}{l_2 - l_1}$.

Applying an IFFT to the CFR yields an estimate of the CIR:

$$\hat{h}[n] = \frac{1}{N} \sum_{k=0}^{N-1} \hat{H}[k] w[k] e^{j2\pi kn/N} \tag{12}$$

where $w[k]$ is a Hann window used to reduce sidelobe effects after inverse fast Fourier transform (IFFT). The estimated CIR $\hat{h}[n]$ is a discrete-time sequence encoding amplitude and delay information of the multipath channel. Multipath parameters such as RSS denoted by P_r and root mean square delay spread (RMS-DS) denoted by τ_{RMS} are extracted from $\hat{h}[n]$:

$$P_r = 10 \log_{10} \left(\sum_k |\alpha_k|^2 \right) \tag{13}$$

$$\tau_{\text{RMS}} = \sqrt{\left(\sum_{k=1}^{K} p_k (t_k - \mu)^2 \right) \Bigg/ \left(\sum_{k=1}^{K} p_k \right)} \tag{14}$$

where t_k and $p_k = |h_k|^2$ denote the arrival time and power of the k-th path, μ is the power-weighted average arrival time.

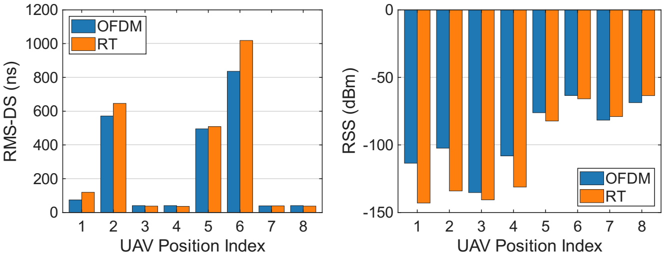

(a) RMS-DS of OFDM and RT

(b) RSS of OFDM and RT

Fig. 2. Validation of OFDM-based channel sounder consistency

The fidelity of the OFDM-based channel sounder was validated by comparing the estimated multipath parameters with RT-generated ground truth. Fig. 2(a) shows that the τ_{RMS} estimates correlate with RT-generated values with correlations up to 0.9957 across all UAV links and a maximum deviation below 15ns, confirming the sounder's accuracy in capturing delay characteristics in this complex environment. Fig. 2(b) shows similarly high consistency for the P_r estimates, with correlations up to 0.9811. The close agreement for both parameters indicates that the implemented OFDM system provides reliable channel measurements for subsequent localization.

III. TERRAIN-DRIVEN LOCALIZATION FRAMEWORK

A. TD-XGBoost Model

In mountainous environments, terrain strongly influences signal characteristics. Localization that depends solely on signal parameters may overlook propagation fading and produce localization errors. Elevation data supplied by DEMs enables the derivation of environmental attributes such as terrain roughness, LoS visibility, and scatter-point distribution. These attributes can function as environmental fingerprints to constrain and correct positioning models. Given the user's uncertainty region Ψ_u discretized into M rectangular grid cells $\mathcal{G} = \{G_i\}_{i=1}^{M}$, we model signal propagation parameters as functions of terrain features. For each grid cell G_i and UAV position $\mathbf{p}_a$, we predict:

$$\begin{cases} P_r(\mathbf{p}_a, G_i) = f_{\theta_r}(\Phi(\mathbf{p}_a, G_i)) \\ \tau_{\text{RMS}}(\mathbf{p}_a, G_i) = f_{\theta_\tau}(\Phi(\mathbf{p}_a, G_i)) \end{cases} \tag{15}$$

where $\Phi(\cdot)$ extracts terrain features from DEM, f_{θ_r} and f_{θ_τ} are XGBoost models, parameterized by θ_r and θ_τ respectively.

The vector $\Phi(\mathbf{p}_a, G_i)$ combines geometric and terrain-specific attributes:

- **Geometric**: Euclidean distance d and relative height h.
- **Path**: LoS/NLoS status (computed via Bresenham's algorithm), obstacle height h_{obs}, and obstacle distance d_{obs}.
- **Terrain morphology**: Average/maximum elevation, average/maximum slope, and terrain roughness σ_z
- **Propagation**: Free-space path loss L_{FS}, Fresnel zone radius r_F, effective path length d_{eff}, and obstruction severity ζ.

Among them, terrain roughness σ_z, free-space path loss L_{FS}, Fresnel zone radius r_F, effective path length d_{eff}, and obstruction severity ζ are derived features. ζ depends on h_{obs} and d_{obs}, and d_{eff} depends on d and h_{obs}. To account for distinct propagation mechanisms, we train separate TD-XGBoost models for LoS and NLoS conditions:

$$f_\theta(\Phi(\mathbf{p}_a, G_i)) = \begin{cases} f_\theta^{\text{LoS}}(\Phi(\mathbf{p}_a, G_i)) & \text{if } \mathbb{I}(\Phi(\mathbf{p}_a, G_i)) = 1 \\ f_\theta^{\text{NLoS}}(\Phi(\mathbf{p}_a, G_i)) & \text{otherwise} \end{cases} \tag{16}$$

where $\mathbb{I}$ is determined by terrain visibility analysis.

Each model is an ensemble of K regression trees:

$$f_\theta(\Phi(\mathbf{p}_a, G_i)) = \sum_{k=1}^{K} f_k(\Phi(\mathbf{p}_a, G_i)), \quad f_k \in \mathcal{F} \tag{17}$$

where $\mathcal{F} = \{f(\mathbf{x}) = w_{q(\mathbf{x})}\}$ denotes the space of regression trees with structure q and leaf weights w. The model is trained by minimizing the following regularized objective:

$$\mathcal{L}(\theta) = \sum_{i=1}^{n} l(y_i, \hat{y}_i) + \sum_{k=1}^{K} \Omega(f_k) \tag{18}$$

$$\Omega(f) = \gamma T + \frac{1}{2}\lambda \|w\|^2 \tag{19}$$

where $l(y_i, \hat{y}_i)$ is a differentiable loss function and $\Omega(f_k)$ regularizes model complexity; specifically, $\Omega(f) = \gamma T + \frac{1}{2}\lambda\|w\|^2$, where T is the number of leaves and γ, λ control tree complexity and weight magnitude.

Performance is evaluated using the physical-scale root mean square error (RMSE):

$$\text{RMSE} = \sqrt{\frac{1}{N}\sum_{i=1}^{N}\left(g^{-1}(\hat{y}_i) - g^{-1}(y_i)\right)^2} \tag{20}$$

where g^{-1} denotes the inverse transformation of P_r (dB to linear scale) and τ_{RMS}, ensuring the error metric reflects physical units rather than scaled values.

Fig. 3 compares the RMSE of feature parameter predictions between the TD-XGBoost and the Random Forest (RF) model under various scenarios. The results demonstrate that TD-XGBoost achieves superior performance in NLoS environments, particularly for RMS-DS. Although both models exhibit comparable performance in RSS prediction, the enhanced capability of TD-XGBoost in capturing complex temporal dependencies makes it more suitable for practical NLoS communication systems.

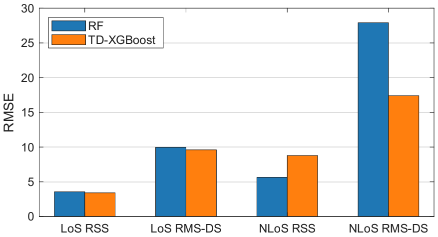

Fig. 3. Comparison of RMSE predicted by TD-XGBoost and RF model

B. Particle-Filter Localization

Algorithm 1: Particle Filter Localization

```
Input: DEM, $\hat{\mathbf{p}}_u$, $\mathbf{p}_a$, TD-XGBoost model $\theta$, maxIter
Output: Estimated position $\hat{\mathbf{p}}'_u \in \mathbb{R}^{1\times 3}$
Initialize $N_p$ particles with uniform distribution, positions $\mathbf{x}_0 \in \mathbb{R}^{N_p\times 3}$, weights $\mathbf{w}_0 \in \mathbb{R}^{N_p\times 1}$
Initialize estimated user position: $\hat{\mathbf{p}}'_u = \mathbf{w}_0^T\mathbf{x}_0$
for $t = 1 \rightarrow maxIter$ do
    Update motion noise: noise $= 25e^{-0.2t}$
    Update particle positions: $\mathbf{x}_t \leftarrow \mathbf{x}_{t-1} + \text{noise}$
    Penalize out-of-bound particles:
      $\mathbf{w}_t^{(\text{outidx})} \leftarrow 10^{-20} * \mathbf{w}_{t-1}^{(\text{outidx})}$
    for $i = 1 \rightarrow N_p$ do
        for $a = 1 \rightarrow N_u$ do
            Compute path features $\Phi(\mathbf{p}_{a,j}, \mathbf{x}_t^{(i)})$
            Predict $\hat{P}_r, \hat{\tau_{\text{RMS}}} \leftarrow f_\theta(\Phi(\mathbf{p}_{a,j}, \mathbf{x}_t^{(i)}))$
            Calculate errors $E_{\text{RSS}}$, $E_{\text{RMS}}$
            Calculate RSS and RMS likelihood:
            $\ell_{P_r}^{(a)} = \frac{\Gamma\left(\frac{\nu+1}{2}\right)}{\sqrt{\nu\pi}\cdot\Gamma\left(\frac{\nu}{2}\right)} \cdot \left(1 + \frac{(E_{\text{RSS}}/\sigma)^2}{\nu}\right)^{-\frac{\nu+1}{2}}$
            $\ell_{\tau_{\text{RMS}}}^{(a)} = \frac{\Gamma\left(\frac{\nu+1}{2}\right)}{\sqrt{\nu\pi}\cdot\Gamma\left(\frac{\nu}{2}\right)} \cdot \left(1 + \frac{(E_{\text{RMS}}/\sigma)^2}{\nu}\right)^{-\frac{\nu+1}{2}}$
            Update particle weight: $w_t^{(i)} \leftarrow w_t^{(i)} \cdot \ell_{P_r}^{(a)} \cdot \ell_{\tau_{\text{RMS}}}^{(a)}$
        end
    end
    Normalize weights: $\mathbf{w}_t \leftarrow \mathbf{w}_t / \sum w_t^{(i)}$
    Calculate effective sample size: EffSamp $= \frac{1}{\sum {w_t^{(i)}}^2}$
    if $EffSamp < 0.3N_p$ then
        Perform resampling
    end
    Calculate estimated position change:
      posChange $= \mathbf{w}_t^T\mathbf{x}_t - \hat{\mathbf{p}}_u$
    Update estimated position: $\hat{\mathbf{p}}_u = \mathbf{w}_t^T\mathbf{x}_t$
    if $posChange < Thresh$ & $t > 5$ then
        break
    end
end
```

To achieve robust localization in complex mountainous environments, we propose a particle filter approach that integrates the TD-XGBoost model, as shown in Algorithm 1. The core innovation lies in utilizing TD-XGBoost-predicted signal parameters as priors for the observation likelihood model while employing a heavy-tailed Student's t-distribution to model observation errors, thereby effectively mitigating the impact of outliers caused by NLoS propagation and multipath effects.

The algorithm approximates the posterior probability distribution of the system state using a set of weighted random samples. We define the UE's position state as $\mathbf{x}_t = [\phi, \lambda]^T$. Given the time-series observations $\mathbf{z}_{1:t}$ (P_r and τ_{RMS}) obtained from UAVs, the algorithm employs N_p particles $\{\mathbf{x}_t^{(i)}, w_t^{(i)}\}_{i=1}^{N_p}$ to approximate the posterior distribution $p(\mathbf{x}_t|\mathbf{z}_{1:t})$. The al-

TABLE I
LIST OF KEY SIMULATION PARAMETERS

Parameter	Value
Surface Conductivity ϵ_c	0.003S/m
Relative Permittivity ϵ_r	17
Max. # of reflections R	3
Max. # of diffractions D	1
Frequency f_k	1.5GHz
Transmit power P_t	30dBm
Subcarrier number N	960
Subcarrier spacing Δf	15kHz
Cyclic prefix length L_{cp}	144
Sampling rate f_n	30.72×10^6
SNR	25

gorithm follows the recursive Bayesian filtering paradigm, comprising two core steps:

- **Prediction step**:
$$p(\mathbf{x}_t|\mathbf{z}_{1:t-1}) = \int p(\mathbf{x}_t|\mathbf{x}_{t-1})p(\mathbf{x}_{t-1}|\mathbf{z}_{1:t-1})d\mathbf{x}_{t-1}$$
where $p(\mathbf{x}_t|\mathbf{x}_{t-1})$ denotes the state transition model.
- **Update step**:
$$p(\mathbf{x}_t|\mathbf{z}_{1:t}) = \eta_t^{-1}p(\mathbf{z}_t|\mathbf{x}_t)p(\mathbf{x}_t|\mathbf{z}_{1:t-1})$$
where η_t normalizes the posterior.

The key innovation is a terrain-adaptive observation-likelihood model. For each particle $\mathbf{x}_t^{(i)}$, the likelihood of observing $\mathbf{z}_t$—P_r and τ_{RMS} from UAV—is computed as:

$$p(\mathbf{z}_t|\mathbf{x}_t^{(i)}) = \prod_{a=1}^{N_U} \ell_{P_r}^{(a)} \ell_{\tau_{\text{RMS}}}^{(a)} \tag{21}$$

where N_U is the number of all positions where a UAV has stopped, and for each position a:

$$\ell_{P_r}^{(a)} = \mathcal{T}\left(\Delta P_r^{(a)}; \sigma_{P_r}, \nu_{P_r}\right) \tag{22}$$

$$\ell_{\tau_{\text{RMS}}}^{(a)} = \mathcal{T}\left(\Delta \tau^{(a)}; \sigma_{\tau}, \nu_{\tau}\right) \tag{23}$$

The terms are defined as follows:

- $\Delta P_r^{(a)} = \hat{P_r}^{(a)} - P_r{}^{(a)}$: residual between measured and predicted P_r for position a.
- $\Delta \tau^{(a)} = \hat{\tau_{\text{RMS}}}^{(a)} - \tau_{\text{RMS}}{}^{(a)}$: residual between measured and predicted τ_{RMS} for position a.
- $\mathcal{T}(x; \sigma, \nu)$: Student's t-distribution evaluated at x with scale parameter σ and degrees of freedom ν.
- $\sigma_{P_r}, \sigma_\tau$: scale parameters for $\Delta P_r^{(a)}$ and $\Delta \tau^{(a)}$.
- $\nu_{\text{RSS}}, \nu_\tau$: degrees-of-freedom parameters controlling tail heaviness.

The predicted values $\hat{P_r}^{(a)}$ and $\hat{\tau_{\text{RMS}}}^{(a)}$ are obtained from the TD-XGBoost model in Section III-A, conditioned on the particle position $\mathbf{x}_t^{(i)}$ and UAV position $\mathbf{p}_a$. Using Student's t-distribution instead of the Gaussian for the likelihood increases robustness to outliers. Its heavier tails better accommodate non-Gaussian errors common in mountainous environments from multipath effects and NLoS conditions.

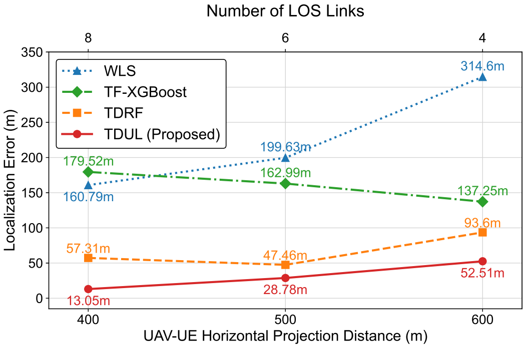

Fig. 4. Impact of UAV-UE horizontal projection distance and number of LoS links on localization errors

IV. PERFORMANCE EVALUATION

A. System Setup and Benchmark Methods

The UE and the UAV are located at altitudes of 1.5m and 50m, respectively, above the mountainous terrain. Detailed RT parameters and OFDM system configurations are given in Table I. To validate the proposed TDUL framework's performance in complex mountainous environments, we benchmarked it against the following methods:

- **WLS**: RSS-based localization using weighted least squares.
- **TF-XGBoost**: Terrain-Free XGBoost trained on basic geometric features (distance, relative height) and signal measurements, excluding terrain-specific attributes.
- **TDRF**: Terrain-Driven localization using RF model.

B. Localization Performance

Fig. 4 illustrates the localization errors of four methods under varying numbers of LoS links in mountainous environment. TDUL outperforms all baselines. With only four LoS links, TDUL attains a minimum error of 52.51m. This corresponds to reductions of 262.09m, 84.74m, and 41.09m relative to WLS, TF-XGBoost, and TDRF, respectively.

Furthermore, TF-XGBoost shows degraded localization performance as the number of LoS links increases (from 137.25 m to 179.52 m). This deterioration arises because TF-XGBoost neglects the influence of mountainous terrain. As LoS links increase, the model persistently produces overly optimistic RSS predictions, introducing systematic errors that undermine the particle filter's weight update. Therefore, in complex terrain, simply increasing the number of links is not enough; terrain-specific attributes must also be taken into consideration.

C. Generalization Ability

To evaluate the generalization capability of the proposed localization framework, the model trained exclusively on valley terrain was deployed on two previously unseen terrains: a valley as shown in Fig. 5(a) and a ridge as shown in Fig. 5(c). The experimental configuration remained identical for both deployments. Fig. 5(b) and Fig. 5(d) illustrate the roughness of the valley and ridge terrains, alongside the particle distribution and weights employed in the filtering algorithm. Specifically,

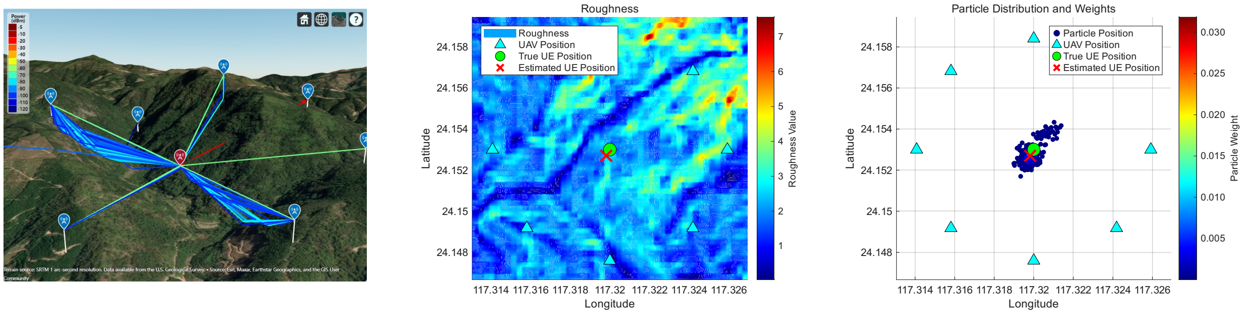

(a) RT results in valley terrain

(b) Localization result (error = 38.74m) in valley terrain

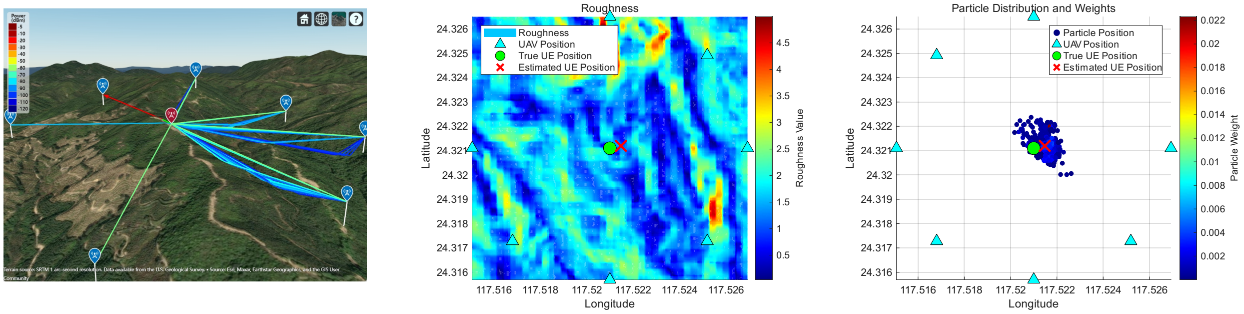

(c) RT results in ridge terrain

(d) Localization result (error = 49.04m) in ridge terrain

Fig. 5. Generalization performance analysis (valley & ridge terrains)

the measured localization errors are 38.74m in valley terrain and 49.04m in ridge terrain. These results across markedly different mountainous topographies indicate the framework's robust adaptability and strong generalization for localization in diverse mountainous environments.

V. CONCLUSION AND FUTURE WORK

The TDUL framework proposed in this paper is designed for UAV-assisted IoT localization in remote mountainous environments. It systematically integrates RT-based physical propagation modeling, realistic communication system simulation, machine-learning prediction, and Bayesian filtering. Future work includes validating the model with field measurements in realistic IoT deployments and extending the framework to dynamic M2M tracking scenarios.

REFERENCES

[1] Y. Zhang, Y. Xie, L. Wang, M. Liwang, and X. Wang, "Reconfigurable intelligent surface enhanced wireless localization: Phase optimization for malicious interference mitigation," *IEEE Trans. Commun.*, pp. 1–1, 2025.

[2] Z. Wang, R. Liu, Q. Liu, L. Han, J. S. Thompson, Y. Lin, and W. Mu, "Toward reliable uav-enabled positioning in mountainous environments: System design and preliminary results," *IEEE Trans. Reliab.*, vol. 71, no. 4, pp. 1435–1463, 2022.

[3] Z. Wang, R. Liu, Q. Liu, L. Han, and J. S. Thompson, "Feasibility study of uav-assisted anti-jamming positioning," *IEEE Trans. Veh. Technol.*, vol. 70, no. 8, pp. 7718–7733, 2021.

[4] Z. Yang, S. Bi, and Y.-J. A. Zhang, "Deployment optimization of dual-functional uavs for integrated localization and communication," *IEEE Trans. Wirel. Commun.*, vol. 22, no. 12, pp. 9672–9687, 2023.

[5] T. Liang, T. Zhang, Q. Wu, W. Liu, D. Li, Z. Xie, D. Li, and Q. Zhang, "Age of information based scheduling for uav aided localization and communication," *IEEE Trans. Wirel. Commun.*, vol. 23, no. 5, pp. 4610–4626, 2024.

[6] J. Luo, T. Liang, C. Chen, and T. Zhang, "A uav mounted ris aided communication and localization integration system for ground vehicles," in *2022 IEEE International Conference on Communications Workshops (ICC Workshops)*, 2022, pp. 139–144.

[7] c. Yapar, R. Levie, G. Kutyniok, and G. Caire, "Real-time outdoor localization using radio maps: A deep learning approach," *IEEE Trans. Wirel. Commun.*, vol. 22, no. 12, pp. 9703–9717, 2023.

[8] D. Ebrahimi, S. Sharafeddine, P.-H. Ho, and C. Assi, "Autonomous uav trajectory for localizing ground objects: A reinforcement learning approach," *IEEE Trans. Mob. Comput.*, vol. 20, no. 4, pp. 1312–1324, 2021.

[9] W. Zhang and W. Zhang, "An efficient uav localization technique based on particle swarm optimization," *IEEE Trans. Veh. Technol.*, vol. 71, no. 9, pp. 9544–9557, 2022.

[10] X. Jing, F. Liu, C. Masouros, and Y. Zeng, "Isac from the sky: Uav trajectory design for joint communication and target localization," *IEEE Trans. Wirel. Commun.*, vol. 23, no. 10, pp. 12 857–12 872, 2024.

[11] S. Gu, C. Luo, Y. Luo, and X. Ma, "Jointly optimize throughput and localization accuracy: Uav trajectory design for multiuser integrated communication and sensing," *IEEE Internet Things J.*, vol. 11, no. 24, pp. 39 497–39 511, 2024.

[12] Y. Dong, C. He, and Z. J. Wang, "Dynamic object tracking by multi-uav with time-variant radio maps," *IEEE Trans. Wirel. Commun.*, vol. 23, no. 7, pp. 7471–7487, 2024.

[13] S. Bi, Z. Zhuo, X.-H. Lin, Y. Wu, and Y.-J. A. Zhang, "Physical-environment-map-aided 3-d deployment optimization for uav-assisted integrated localization and communication in urban areas," *IEEE Internet Things J.*, vol. 11, no. 9, pp. 15 490–15 503, 2024.

[14] J. Chen, U. Mitra, and D. Gesbert, "3d urban uav relay placement: Linear complexity algorithm and analysis," *IEEE Trans. Wirel. Commun.*, vol. 20, no. 8, pp. 5243–5257, 2021.

[15] F. Zhou, L. Fan, J. Tang, and W. Chen, "Placement and concise mse lower-bound for uav-enabled localization via rss," *IIEEE Trans. Veh. Technol.*, vol. 71, no. 2, pp. 2209–2213, 2022.